FLUID FLOW AND HEAT TRANSFER IN A LAMINAR RADIAL IMPINGING JET

S. CHAKRABORTY*, S. P. SENGUPTA* AND G. BISWAS†

* Department of Chemical Engineering, Indian Institute of Technology, Kharagpur, India
† Department of Mechanical Engineering, Indian Institute of Technology, Kanpur, India

ABSTRACT

From the solution of full Navier–Stokes and energy equations, the development of the flow field and heat transfer characteristics in a radial jet reattachment flow have been analysed. The influence of Reynolds number of re-attachment length for the case of steady laminar flows has been determined. However, beyond a Reynolds number of 250, the flow field becomes unsteady and has been found to have a periodic nature. This periodic flow has been found to persist up to a Reynolds number of 750. The periodicity has been characterized by the Strouhal number which shows a slight but continuous variation with Reynolds number around a value of 0.12. The point of maximum heat transfer is within the re-attachment zone in the range of Reynolds numbers studied.

KEY WORDS Navier–Stokes Heat transfer Radial jet Separation

NOMENCLATURE

b nozzle width

C_f skin friction coefficient, $2\mu\left(\dfrac{\partial v}{\partial x}\right)_w\Big/ \rho V_{av}^2$

c_p specific heat of fluid

h heat transfer coefficient, $-k(\partial T/\partial x)_w/(T_w - T_\infty)$

k thermal conductivity of the fluid

Nu   local Nusselt number, hb/k

p pressure

P nondimensional pressure, $p/\rho V_{av}^2$

Pr   Prandtl number, $\mu c_p/k$

r radial dimension of coordinates

R r/b

Re   Reynolds number, $V_{av}b/v$

Ro   dimensionless radial distance at the end of the computational domain

R_r re-attachment length on the flat surface

S Strouhal number, fb/V_{av}

T temperature

$T\Delta$ time level

t time

t nondimensional time, $t/(b/V_{av})$

u axial component of velocity

U nondimensional axial velocity, u/V_{av}

v radial component of velocity

V nondimensional radial velocity, v/V_{av}

x axial dimension of coordinate

X x/b

Greek letters

θ dimensionless temperature, $(T - T_\infty)/(T_w - T_\infty)$

ϕ azimuthal dimension of cylindrical polar coordinate

μ dynamic viscosity of the fluid

v kinematic viscosity of the fluid

ρ density of the fluid

τ shear stress, $\mu\left(\dfrac{\partial v}{\partial x}\right)$

Subscripts

w at the plate wall

∞ condition at the exit of the nozzle

av average

INTRODUCTION

Impinging jet heat transfer finds its applications in a number of areas. Flow structure and heat transfer in impinging jets have been well documented and discussed by Martin[1]. Of the articles describing the details of the flow region in an impinging jet, the investigations of Glauert[2], Gardon and Akfirat[3], and Sparrow and Lee[4] need special mention. However, it was pointed out that if the jet and the surroundings are of the same fluid, then there is a substantial amount of mixing between the jet and the surrounding fluid. Heiningen et al.[5] and Saad et al.[6] reported flow and heat transfer characteristics for two dimensional and axisymmetric submerged jets, respectively. The mixing between the jet and the quiescent fluid is even better in the case of submerged radial jets. Radial jets were investigated by Squire[7] and Heskestad[8]. Thereafter, however, radial jets had received relatively little attention by researchers – perhaps due to the relatively lower heat transfer coefficient in the stagnation region as compared to that in axial jets. Only in recent years various aspects of radial jets are being investigated because of their ability to re-attach on the adjacent surfaces and produce separated flow patterns beneficial for industrial applications.

With the advent of modern high speed computers, the heat removal rate from the integrated circuit packages (icp's) and other electronic components has occupied a decisive role in electronic cooling. Due to miniaturization, the size of the electronic components has become very small, the heat flux has become significantly high (of the order of 500 kW/m^2) and the need for cooling such high heat-release-component functionally has become very important. Cooling of integrated circuit packages and other components by impinging jets is a prevalent practice, Womac et al.[9]. However, the spread of the straight impinging jet is limited to a small region although the heat removal rate is significantly high. In order to increase the spread of the impinging jet, without sacrificing much of the objective of a high heat removal rate from the heat generating surface, radial jets, have been found to be an acceptable alternative. Due to self sustained oscillations in the case of high Reynolds number radial jets, the point of maximum heat transfer swings over a fairly large radial distance. Experimental studies on heat transfer with submerged radial jets have been conducted by Page et al.[10] and Ostowari et al.[11]. A theoretical analysis of the re-attachment flow due to turbulent radial jets can be found in Page et al.[12]. However, detailed flow field information describing basic mechanisms involved in re-attachment is not available. In this paper, a computational study has been undertaken to perform numerical flow visualization through the solution of the full Navier–Stokes equations and to investigate heat transfer characteristics on the flat surface due to radial jet impingement.

Figure 1 illustrates the flow model of a radial jet impinging on a flat surface. A cylindrical coordinate system r–ϕ–x, where r denotes the radial distance from the axis of symmetry (x-axis),
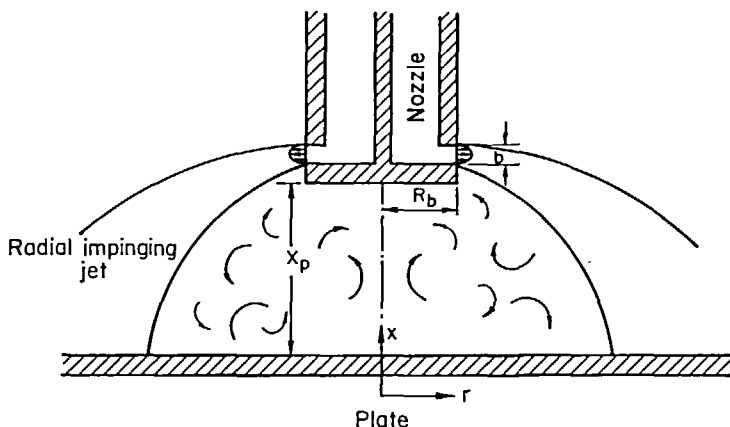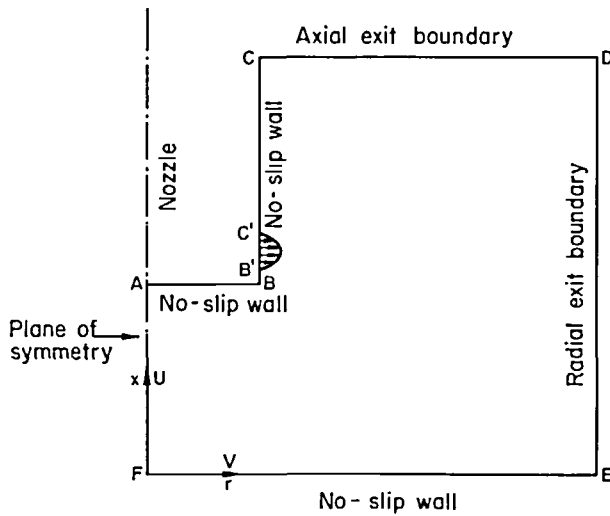

Figure 1 Flow model for radial impinging jet

Figure 2 Computational domain

is chosen. Flow is assumed to be independent of the variation in ϕ which yields a two dimensional condition, as shown in *Figure 2*. The computational domain is *ABCDEFA* where the nozzle exit velocity is described by the velocity profile at *B'C'*.

FLOW MODEL

The following assumptions were made in the development of the model:

(a) Incompressible flow for the laminar submerged radial jet;
(b) The velocity profile at the exit of the nozzle is $v = v(x)$, *for $B' \leqslant x \leqslant C'$*;
(c) The momentum equations are unsteady incompressible and laminar.

In practice, the flow becomes turbulent for a high exit velocity of the fluid from the nozzle. However, the critical value of the flow velocity for transition to turbulent flow is not clearly known. We have considered the unsteady Navier–Stokes equation as the governing equation set since it provides information regarding the transition from steady laminar to unsteady periodic and then from unsteady periodic to unsteady chaotic/turbulence.

BASIC EQUATIONS AND METHOD OF SOLUTION

The computational domain has already been described in *Figure 2*. Cylindrical axisymmetric coordinates have been used. The velocity components u and v are in coordinate directions x and r, respectively. The basic equations for computation are the continuity, unsteady Navier–Stokes and the energy equations. In nondimensional forms they are:

$$D \equiv \frac{\partial V}{\partial R} + \frac{\partial U}{\partial X} + \frac{V}{R} = 0 \tag{1}$$

$$\frac{\partial V}{\partial t} + \frac{\partial (UV)}{\partial X} + \frac{\partial V^2}{\partial R} + \frac{V^2}{R} = -\frac{\partial P}{\partial R} + \frac{\nabla^2 V}{\text{Re}} \tag{2}$$

$$\frac{\partial V}{\partial t} + \frac{\partial UV}{\partial R} + \frac{\partial U^2}{\partial X} + \frac{UV}{R} = -\frac{\partial P}{\partial X} + \frac{\nabla^2 U}{\mathrm{Re}} \qquad (3)$$

$$\frac{\partial \theta}{\partial t} + V\frac{\partial \theta}{\partial R} + U\frac{\partial \theta}{\partial X} = \frac{\nabla^2 \theta}{\mathrm{Re}\cdot\mathrm{Pr}} \qquad (4)$$

In the above equations, the velocity has been nondimensionalized with the average incoming velocity V_{av} at the exit from the nozzle, linear dimensions have been nondimensionalized by b, the width of the nozzle, and pressure by ρV_{av}^2 and the nondimensionalized temperature is defined as $\theta = (T - T_\infty)/(T_w - T_\infty)$. T_∞ is the fluid temperature at the nozzle exit, T_w is temperature of the plate which is higher than that of the fluid and T is the dimensional temperature. No-slip boundary conditions for velocities on all solid surfaces are used. At the exit from the nozzle the axial, u, component of the velocity is assumed to be zero and a parabolic or uniform profile for the radial velocity, v, is deployed. A vanishing shear condition is used at the axis of symmetry. The temperature of the plate is constant and the temperature of the fluid at the nozzle exit is assumed to be uniform. At the radial and axial exit planes of the computational domain, the boundary conditions for the dependent variables are obtained by setting the second derivatives in the R and X direction equal to zero. These are called continuative outflow boundary conditions and they ensure smooth transition through the exit planes of the computational domain.

However, under some conditions, there is fluid inflow over the outflow boundary. Perhaps, the best strategy, for such a case, would be to extend the solution domain to sufficiently large radii so that there is no back-flow at the exit plane. A close examination reveals that the boundary conditions at the exit plane do not forcefully impose any global mass balance. An additional constraint on pressure has been sought and constant pressure at the exit is used. This, along with some extrapolations of the exit velocities from the interior points through continuative boundary conditions, allows velocity correction at the exit without directly imposing the global continuity condition.

A modified version of Marker and Cell (MAC) method due to Harlow and Welch[13], Hirt and Cook[14] is used to obtain the numerical solutions of equations (1) through (4). The computational domain is divided into Cartesian cells. Staggered grid arrangements are used in which velocity components are defined at the centre of the cell faces to which they are normal, *Figure 3*. The pressure and temperature are defined at the centre of the cells. A detailed discussion of the numerical procedure is given in Biswas *et al.*[15] and Mukhopadhyay *et al.*[16]. However, a concise description is being provided for clarity. MAC is a semi-implicit finite difference technique consisting of two steps. In the first step, the momentum equations are solved explicitly in order
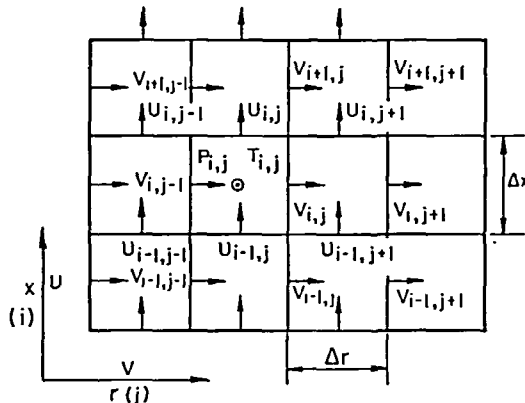

Figure 3 Staggered grid showing the location of discretized variables

to obtain a provisional velocity field from a given velocity and pressure field. In the second step, the continuity equation is implicitly solved by a pressure-velocity iteration until the velocity divergence at each cell reaches a preset negligible value. This iteration procedure amounts to an SOR-solution for the Poisson equation for pressure, Brandt et al.[17]. Once the corrected velocity and pressure field has been determined, the energy equation is also solved by an SOR method. The derivatives of the inertia terms were discretized according to the hybrid model, Gentry et al.[18] and Hirt et al.[19], which is basically a weighted average that combines upwind and central differencing to achieve the stability of the upwind method and better formal accuracy of central differencing. The following example, in conjunction with *Figure 3*, illustrates the essence of this discretization scheme. The second term in *r*-momentum equation, $\left[\dfrac{\partial UV}{\partial X}\right]$, is discretized as:

$$\left[\frac{\partial UV}{\partial X}\right]_{i,j} = \frac{1}{4\delta X}\left[(U_{i,j} + U_{i,j+1})(V_{i,j} + V_{i+1,j})\right.$$
$$+ \alpha_p|(U_{i,j} + U_{i,j+1})|(V_{i,j} - V_{i+1,j})$$
$$- (U_{i-1,j} + U_{i-1,j+1})(V_{i-1,j} + V_{i,j})$$
$$\left. + \alpha_p|(U_{i-1,j} + U_{i-1,j+1})|(V_{i-1,j} - V_{i,j})\right] \tag{5}$$

The factor α_p serves to balance the upwind contribution. If α_p, the difference equations are centred in space. In the present paper, the factor was restricted between 0.2 and 0.3 so that the formulation can retain *something* of the second order accuracy, Timin and Esmail[20].

The minimum CPU time for obtaining a solution is 540 s. For these computations a grid of 52 × 42 has been used. For a Reynolds number of 100, computations have been performed with three different grids, viz., 27 × 22, 52 × 42 and 77 × 62. The extrapolated grid-independent average Nusselt number Nu_{av} on the impinging plate differs from the corresponding Nu_{ar} obtained with the coarsest grid by 4.0 percent. Hence further computations have been performed with 52 × 42 grids.

In order to be conclusive regarding the reliability of our discretization scheme, we have tested the scheme for a Lid Driven Square Cavity. *Figure 4* depicts that the computation, with weighted
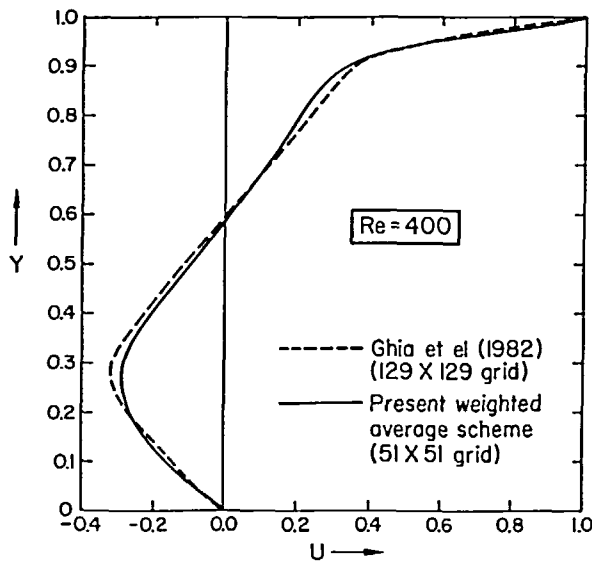

Figure 4 Variation of *U* velocity along the vertical midplane for the lid driven flow in a square cavity

average scheme, on 51 × 51 grids shows good agreement with the result of Ghia et al.[21] who used a 129 × 129 mesh with multigrid technique.

RESULTS AND DISCUSSION

Computations have been performed with various Reynolds numbers. Air has been considered as the working fluid and hence the Prandtl number for this study has been taken as 0.7. *Figures 5(a), (b)* and *(c)* show the velocity profiles at different radial locations in the flow field for three different Reynolds numbers. The re-attachment height, Xp, was kept constant for all the three cases. Formation of a separation bubble and its displacement towards the outward direction along the radius with increasing Reynolds number is quite evident from the illustration. There exists a dead-water-zone directly under the nozzle for all the three cases. However, the radially outward shift of the recirculating zone with increasing Reynolds number is synonymous with the increased re-attachment length with an increase in Reynolds number. *Figures 6(a)* and *(b)* are the corresponding streamlines for the cases shown in *Figures 5(b)* and *(c)*. It may be observed that the induced secondary vortex sucks the cold fluid from across the boundary, entrains it and rolls it over the impinging plate.
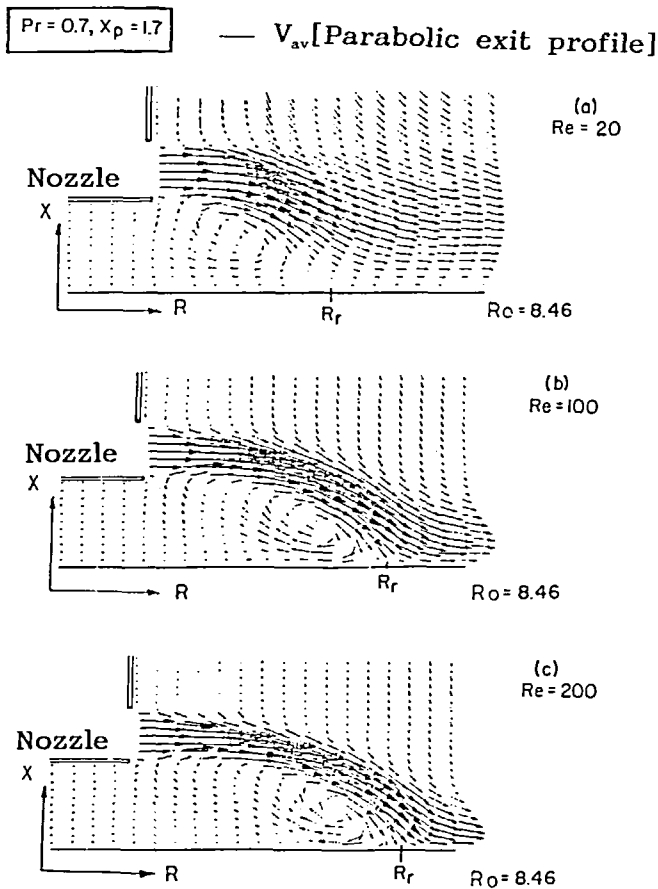

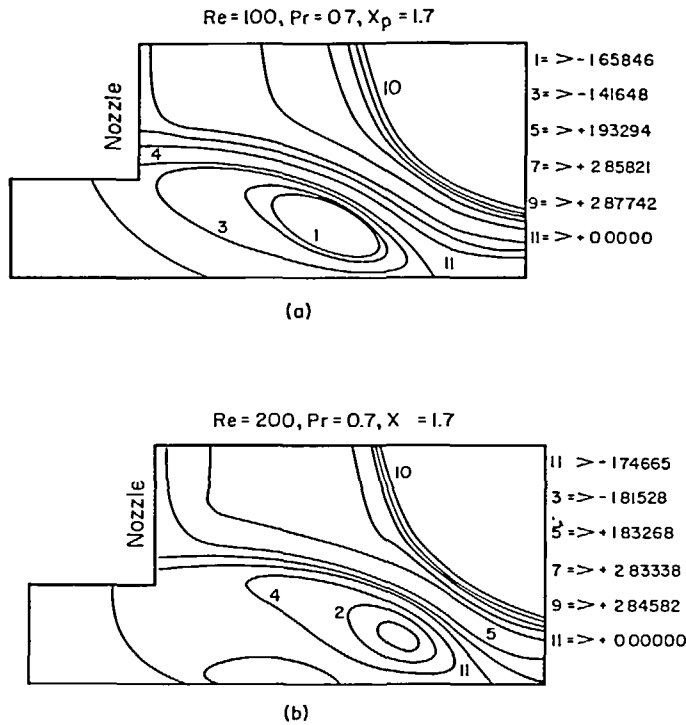*Figure 5* Velocity profiles at different radial locations in the flow field

Re = IOO, Pr = O7, X_p = I.7

| I = > - I 65846 |
| 3 = > - I 41648 |
| 5 = > + I 93294 |
| 7 = > + 2 85821 |
| 9 = > + 2 87742 |
| II = > + 0 0000 |

(a)

Re = 200, Pr = 0.7, X = I.7

| II   > - I 74665 |
| 3 = > - I 81528 |
| 5 = > + I 83268 |
| 7 = > + 2 83338 |
| 9 = > + 2 84582 |
| II = > + 0 00000 |

(b)

Figure 6 Streamlines for a radial jet re-attachment flow

Figures 7(a) and (*b*) show the effect of exit velocity profile of the nozzle on the flow field for the Reynolds number of 20 and 100, respectively. The same qualitative trends of velocity vectors, as observed with the parabolic exit profile in *Figure 5*, are observed here. The recirculation zone shifts radially outward with increasing Reynolds number. Understandably, the quantitative values of the re-attachment length for the same Reynolds number are different for different exit velocity profiles of the nozzle. As an example, for Re = 20, the R_r in case of parabolic exit profile from the nozzle is 5.24 while that for the uniform exit velocity profile from the nozzle is 5.78.

Beyond a Reynolds number of 250, the flow field becomes unsteady. *Figures 8(a)* through *8(c)* present a flow visualization study for Reynolds number of 500 at different time levels. The entrainment and the development of counter-rotating secondary vortices can be discerned in all the plots. In *Figure 8(b)* for time level, $T\Delta = 300$ a sharp dip of jet towards the plate can be observed. The bottom vortex becomes stronger (as compared to that in *Figure 8(a)*) and the jet turns toward the plate. In another time level (*Figure 8(c)*), the bottom vortex gains additional strength which induces entrainment of cold fluid almost axially in the immediate neighbourhood above the vortex. Due to unsteadiness, the re-attachment lengths measured at different time levels are different.

In order to characterize the unsteadiness, the variation of fluctuating velocity, v, with time was traced over an interval of time at a position below the nozzle at $r = 0.1$ in the wake. This approach is after the method of Okajima[22]. *Figure 9* shows the signal traces of the radial velocity component behind the wake. The time period T can be calculated from such signal traces and the corresponding frequency f ($= 1/T$) and Strouhal number S ($= fb/V$) can also be found. However, at a Reynolds number of 750, the flow loses its periodic nature and the unsteadiness is not characterized. As such for Re = 750, the numerical scheme did not work after some 500
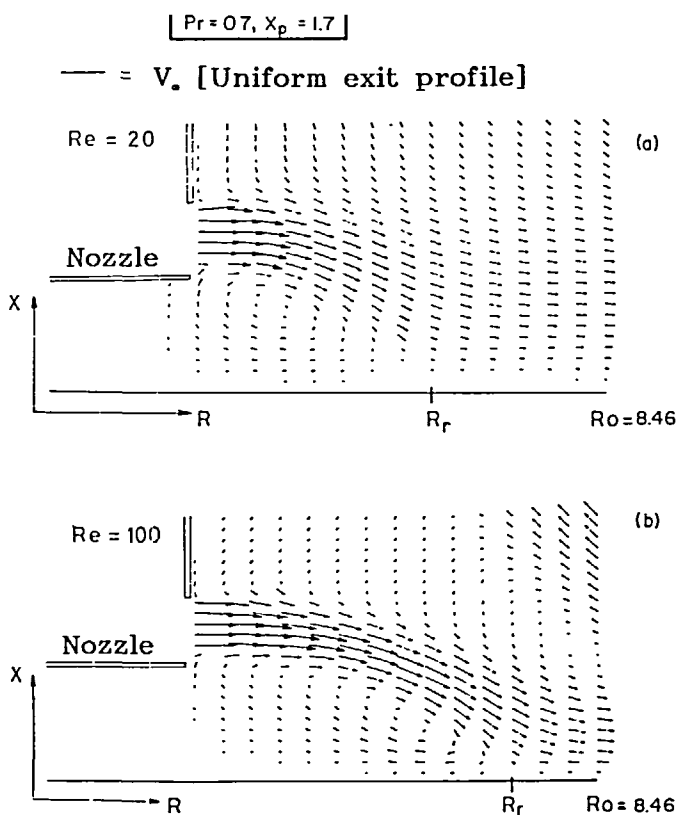
Figure 7   Velocity profiles at different radial locations in the flow field

iterations in the time cycle. It may be said that transition to unsteady chaotic flow takes place somewhere around a Reynolds number of 750. The flow regime which persists between a Reynolds number of 250 and the transition Reynolds number may be termed as unsteady periodic. In this region the periodicity is found to vary with Reynolds number and the Strouhal number shows a continuous but very slight variation around a value of 0.12.

For all steady flow cases, as mentioned earlier, the re-attachment length, the length of the primary bubble separation, for a fixed Reynolds number, did not vary with time. *Figure 10* shows the variation of reattachment length with the Reynolds number for a fixed location of the nozzle above the plate. The reattachment length increases with an increase in Reynolds number.

Figure 11(a) shows the local Nusselt number distribution for various Reynolds number in the steady flow regime. In all cases, a low heat transfer zone exists just below the radial nozzle, followed by a slight trough and then a rapid rise to the maximum near the re-attachment point. Distribution of local skin friction coefficient ($C_f \times Re$) for various Reynolds number is shown in *Figure 11(b)*. At the re-attachment point, the shear stress and consequently the skin friction changes from a negative value to a positive value. Comparing *Figures 11(a)* and *11(b)* we observe that the point of maximum heat transfer occurs just prior to the re-attachment point. This observation is in agreement with the experimental results obtained by Ostowari et al.[11] for high Reynolds number flows.

In conclusion, it can be said that the point of maximum Nusselt number is located within the re-attachment ring. It is also noticed that the maximum heat transfer rate is a strong function

$\boxed{\text{Re} = 500, \ X_p = 1.7}$ $— = V_{av}$[Parabolic exit profile]
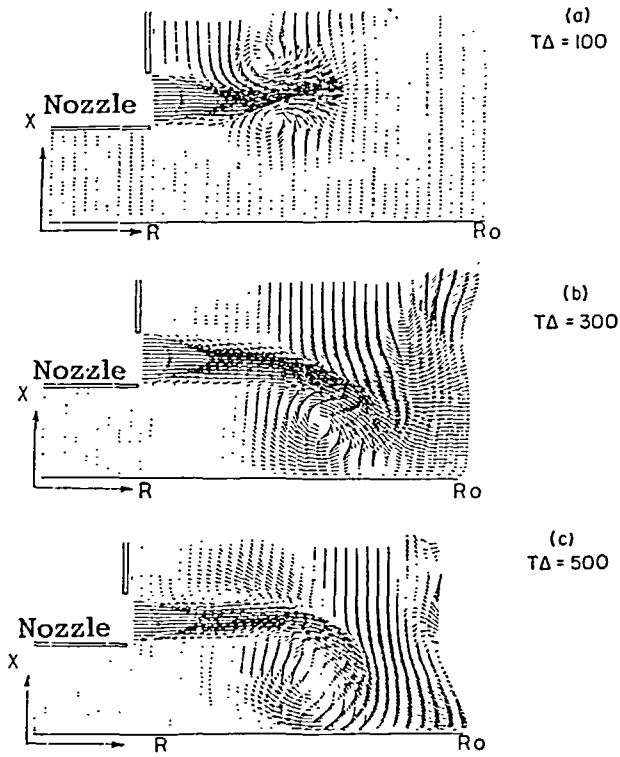

Figure 8   Variation of a flow field at different times
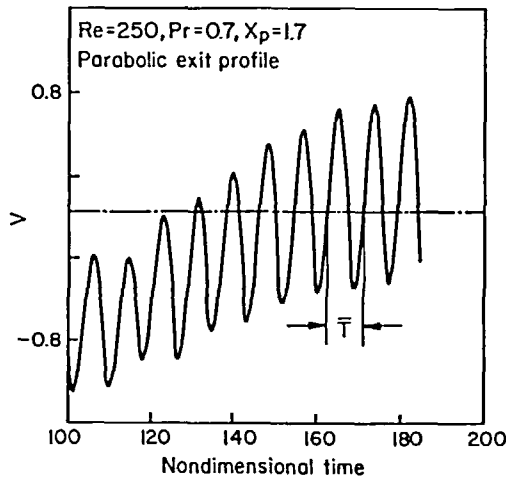

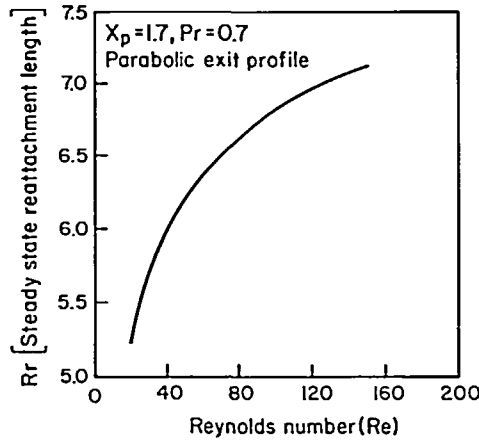Figure 9   Signal traces of the fluctuating velocity component

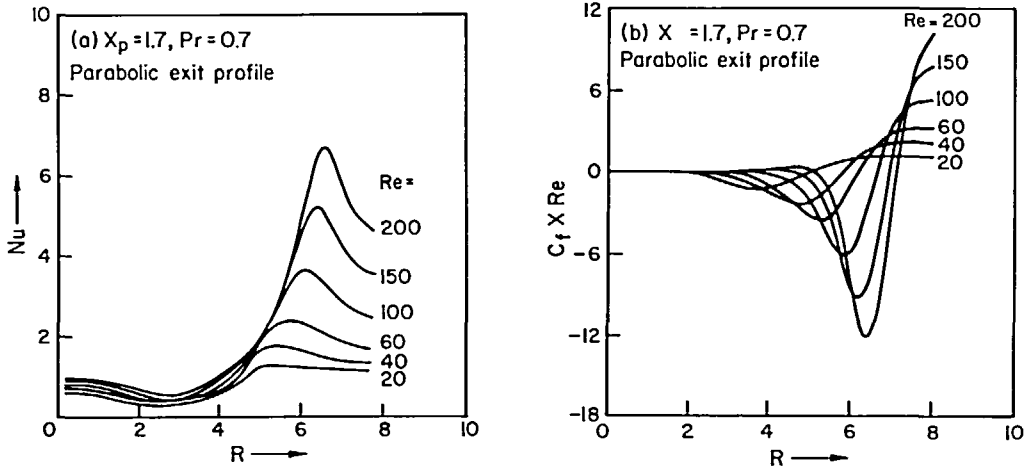*Figure 10*   Re-attachment lengths for different Reynolds numbers

Figure 11   (a) Variation of Nusselt number distribution for various Reynolds numbers (b) Variation of skin friction
$(C_f \times Re)$ on the plate for different values of Reynolds number

of Reynolds number. The highest heat transfer rate takes place at the highest Reynolds number. The point of maximum heat transfer shifts radially outward with increasing Reynolds number which, understandably, is a consequence of the increase in re-attachment length with the increase in Reynolds number.

Figure 12(a) shows the influence of jet-to-plate spacing on heat transfer in the regime of steady flow. The Nusselt number increases with the decrease in X_p. The reason for such a behaviour can be attributed to well known Coanda effect, Tritton[23], which describes the adherence of the jet over the impingement plate in the direction of flow. With the increase in jet-to-plate spacing, the influence of the Coanda effect decreases and beyond a distance $X_p \cong 6$ the flow does not re-attach on the surface. It is also observed that the point of maximum Nusselt number shifts radially outward with increasing jet-to-plate spacing. *Figure 12(b)* shows the effect of jet-to-plate spacing on local skin friction coefficient distribution. It is evident that the skin friction coefficient $(C_f \times Re)$ increases with decrease in jet-to-plate distance. The re-attachment point also shifts radially outward as the jet-to-plate spacing increases. As such, the shift of the point of maximum
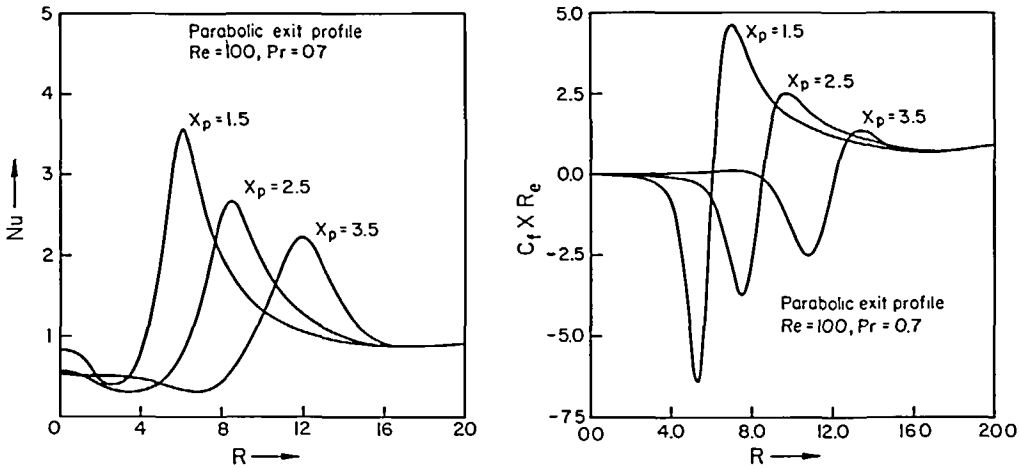
Figure 12 (a) Variation of Nusselt number distribution over the reattaching surface for different nozzle height. (b) Skin friction distribution over the re-attaching surface for different nozzle height
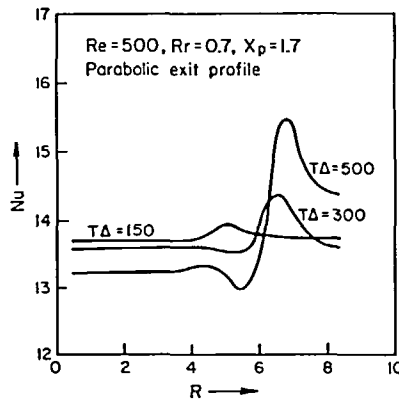

Figure 13 Variation of Nusselt number distribution at different times at a fixed Reynolds number

Nusselt number in the outward direction is brought about by the radially outward shift of the re-attachment point due to increased jet-to-plate spacing.

Figure 13 shows the heat transfer characteristics of an unsteady periodic flow field. In an unsteady flow field, the re-attachment length and the velocity gradients at the plate wall vary with time. As expected, the Nusselt number distribution and the point of maximum heat transfer also vary with time. *Figure 13* shows the time evolution of the local Nusselt number distribution. The Nusselt number distribution for a Reynolds number of 500 at a time level of 500 follows the trend of Ostowari et al.[11]. Due to a sparse experimental data base in the flow regime, a quantitative comparison of the results could not be carried out.

The model validation was performed through a comparison with the published data of Deshpande and Vaishnav[24]. The solution algorithm was used to calculate submerged laminar straight jet impinging on a plane surface and the distribution of $\tau_w/(4\rho V_{av}^2)$ on the impinging surface was compared. *Figure 14* shows the distribution of along the radial direction on the plate. The computed result compares favourably with the result of Deshpande and Vaishnav[24]. The discrepancy lies below ±5 percent.
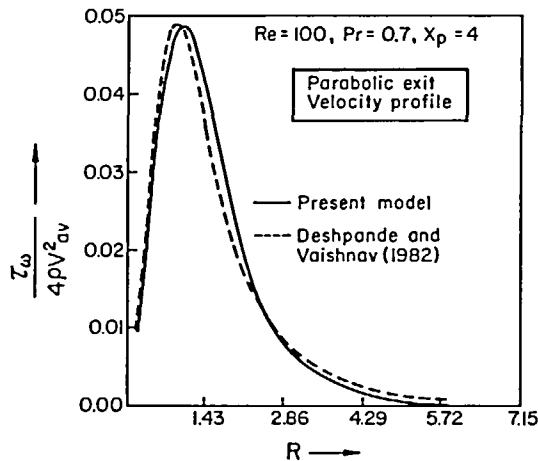
Figure 14   Distribution of $\tau_w/4\rho V_{av}^2$ on the surface for axial impinging jet

CONCLUDING REMARKS

The transfer of heat from the hot plate due to impingement of cold fluid-jet has been investigated. The effect of the governing input parameters, viz., the effect of nozzle exit velocity profile, Reynolds number and the height of the nozzle base from the plate surface has been studied. Beyond a Reynolds number of 250, the flow field becomes unsteady and periodic. The periodicity is characterized by a Strouhal number which showed a slight but continuous variation around a value of 0.12 for a Reynolds number range of 250 to 750. However, in the vicinity of a Reynolds number of 750 the investigation tends to put a limit to the laminar flow model. It is conjectured that transition to chaotic or turbulent flow takes place even before this limit. For all the cases studied as a part of the present investigation, the heat transfer coefficients are small in the recirculation zone immediately below the nozzle, which also comprises of the dead-water zone beyond which the value rises to a maximum value near the re-attaching zone followed by a decay. Further, for the unsteady periodic flow a swing in the location of the peak value was also observed which would increase the spread for the heat transfer as compared to that of a straight jet. Finally, if the nozzle is located at a distance beyond a certain value, the beneficial effects of radial jet impinging heat transfer appear to be lost.

REFERENCES

1 Martin, H. Heat and mass transfer between impinging gas jets and solid surfaces, *Advances in Heat Transfer* (Eds. J. P. Hartnett and T. F. Irvine, Jr.), 13, 1–60 (1977)
2 Glauert, M. B. The wall jet, *J. Fluid Mech.*, 1, 625–643 (1956)
3 Gardon, R. and Akfirat, J. C. The role of turbulence in determining the transfer characteristics of impinging jets, *Int. J. Heat Mass Transfer*, 8, 1261–1272 (1965)
4 Sparrow, E. M. and Lee, L. Analysis of flow field and impingement heat and mass transfer due to a nonuniform slot jet, *J. of Heat Transfer*, 97, 191–197 (1975)
5 Van Heiningen, A. R. P., Majumdar, A. S. and Douglas, W. J. M. Numerical prediction of the flow field and impinging heat transfer caused by a laminar slot jet, *J. of Heat Transfer*, 98, 654–658 (1976)
6 Saad, N. R., Douglas, W. J. M. and Majumdar, A. S. Prediction of heat transfer under an axisymmetric laminar impinging jet, *Ind. Engng. Chem. Fundam.*, 16, 148–154 (1977)
7 Squire, H. B. Radial jets, *50 jhare Grenzschichtforchung*, F. Veweg & Sons, Braunschweig, West Germany, 47–54 (1955)
8 Heskestad, G. Hot wire measurements in a radial turbulent jet, *J. of Applied Mech.*, 33, 417–424 (1966)
9 Womac, D. J., Ramadhyani, S. and Incropera, F. P. Correlating equations for impingement cooling of small heat sources with single circular liquid jets, *J. of Heat Transfer*, 115, 106–115 (1993)

10 Page, R. H. and Ostowari, C. Heat transfer during radial jet attachment, *Proc. of Symp. Heat and Mass Transfer*, University of, Illinois at Urbana Champaign, USA, 1–16 (1987)

11 Ostowari, C., Paikert, B. and Page, R. H. Heat transfer measurements of radial jet re-attachment on a flat plate, *Proc. of the Nat. Fluid Dynamics Congress*, AIAA Paper No. 88-3772 (1988)

12 Page, R. H., Hadden, L. L. and Ostowari, C. A theory for radial jet re-attachment flow, *Proc. of the Nat. Fluid Dynamics Congress*, AIAA Paper No. 88-3589 (1988)

13 Harlow, F. H. and Welch, J. E. Numerical calculation of time dependent viscous incompressible flow of fluid with free surface, *Phys. Fluids*, **8**, 2182–2188 (1965)

14 Hirt, C. W. and Cook, J. L. Calculating three dimensional flows around structures and over rough terrain, *J. Comp. Phys.*, **10**, 324–340 (1972)

15 Biswas, G., Laschefski, H., Mitra, N. K. and Fiebig, M. Numerical investigation of mixed convection heat transfer in a horizontal channel with a built-in square cylinder, *Num. Heat Transfer, Part A*, **18**, 173–188 (1990)

16 Mukhopadhyay, A., Biswas, G. and Sundararajan, T. Numerical investigation of confined wakes behind a square cylinder in a channel, *Int. J. for Num. Meth. Fluids*, **14**, 1473–1484 (1992)

17 Brandt, A., Dendy, J. E., Jr. and Ruppel, H. The multigrid method for semi-implicit hydrodynamic codes, *J. Comp. Phys.*, **34**, 348–370 (1980)

18 Gentry, R. A., Martin, R. E. and Daly, B. J. An Eulerian differencing method for unsteady compressible flow problems, *J. Comp. Phys.*, **1**, 87–118 (1966)

19 Hirt, C. W., Nichols, B. D. and Romero, N. C. SOLA – A numerical solution algorithm for transient fluid flows, *Los Alamos Scientific Lab Report LA-5652* (1975)

20 Timin, T. and Esmail, N. A comparative study of central and upwind difference schemes using the primitive variables, *Int. J. for Num. Meth. in Fluids*, **3**, 295–305 (1983)

21 Ghia, U., Ghia, K. N. and Shin, C. T. High-resolutions for incompressible flow using the Navier–Stokes equations and multigrid method, *J. Comp. Phys.*, **48**, 387–411 (1982)

22 Okajima, A. Strouhal numbers of rectangular cylinders, *Fluid Mech.*, **123**, 379–398 (1982)

23 Tritton, D. J. *Physical Fluid Dynamics*, Von Nostrand Reinhold, UK, 284–286 (1977)

24 Deshpande, M. D. and Vaishnav, R. N. Submerged laminar jet impingement on a plane, *J. Fluid Mech.*, **114**, 213–236 (1982)